Hydrol. Earth Syst. Sci. Discuss., 11, 5327–5365, 2014
www.hydrol-earth-syst-sci-discuss.net/11/5327/2014/
doi:10.5194/hessd-11-5327-2014

Hydrology and Earth System Sciences
Open Access
Discussions

LiDAR measurement of seasonal snow accumulation along an elevation gradient in the southern Sierra Nevada, California

P. B. Kirchner[1,*], **R. C. Bales**[1], **N. P. Molotch**[2,3], **J. Flanagan**[1], **and Q. Guo**[1]

[1]Sierra Nevada Research Institute, University of California, Merced, CA, USA
[2]Department of Geography and the Institute of Arctic and Alpine Research, University of Colorado at Boulder, Boulder, CO, USA
[3]Jet Propulsion Laboratory, California Institute of Technology, Pasadena, CA, USA
[*]now at: Joint Institute for Regional Earth System Science and Engineering, University of California, Los Angeles, CA, USA

Received: 7 April 2014 – Accepted: 15 April 2014 – Published: 21 May 2014

Correspondence to: P. B. Kirchner (peter.b.kirchner@jpl.nasa.gov)

Published by Copernicus Publications on behalf of the European Geosciences Union.

Abstract

We present results from snow-on and snow-off airborne-scanning LiDAR measurements over a 53-km^2 area in the southern Sierra Nevada. We found that snow depth as a function of elevation increased approximately 15 cm 100 m^{-1}, until reaching an elevation of 3300 m, where depth sharply decreased at a rate of 48 cm 100 m^{-1}. Departures from the 15 cm 100 m^{-1} trend, based on 1-m elevation-band means of regression residuals, showed slightly less-steep increases below 2050 m; steeper increases between 2050–3300 m; and less-steep increases above 3300 m. Although the study area is partly forested, only measurements in open areas were used. Below approximately 2050 m elevation, ablation and rainfall are the primary causes of departure from the orographic trend. From 2050 to 3300 m, greater snow depths than predicted were found on the steeper terrain of the northwest and the less-steep northeast-facing slopes, suggesting that ablation, aspect, slope and wind redistribution all play a role in local snow-depth variability. At elevations above 3300 m orographic processes mask the effect of wind deposition when averaging over large areas. Also, terrain in this basin becomes less steep above 3300 m. This suggests a reduction in precipitation from upslope lifting, and/or the exhaustion of precipitable water from ascending air masses. Our results suggest a precipitation lapse rate for the 2100–3300 m range of about 6 cm 100 m^{-1} elevation. This is a higher gradient than the widely used PRISM (Parameter-elevation Relationships on Independent Slopes Model) precipitation products, but similar to that from reconstruction of snowmelt amounts from satellite snowcover data. Our findings provide a unique characterization of the consistent, steep average increase in precipitation with elevation in snow-dominated terrain, using high-resolution, highly-accurate data, as well as the importance of solar radiation, wind redistribution and mid-winter melt with regard to snow distribution.

HESSD
11, 5327–5365, 2014

1 Introduction

In mountainous regions of the western United States snowmelt is the dominant contributor to surface runoff, water use by vegetation and groundwater recharge (Bales et al., 2006; Earman and Dettinger, 2011). Because of the importance of mountain snowpacks and their vulnerability in a warmer climate, several researchers have recently developed scenarios for changes in annual and multiyear mountain water cycles, including, trends in water storage and runoff, groundwater recharge, and feedbacks with vegetation (Peterson et al., 2000; Marks et al., 2001; Lundquist et al., 2005; Maxwell and Kollet, 2008; Barnett et al., 2008; Anderson and Goulden, 2011; Trujillo et al., 2012).

Given the challenges to measuring the spatial distribution of mountain precipitation, the processes controlling its distribution remain poorly understood. However, since a large majority of precipitation in the middle and upper elevations of the southern Sierra Nevada falls and accumulates as snow, with limited ablation through much of the winter, we can examine snow accumulation to assess processes governing the distribution of precipitation.

Snow accumulation across the mountains is primarily influenced by orographic processes, involving feedbacks between atmospheric circulation, terrain and the geomorphic processes of mountain uplift, erosion and glaciation on the earth's surface (Roe, 2005; Roe and Baker, 2006; Pedersen et al., 2010; Kessler et al., 2006; Stolar et al., 2007; Galewsky, 2009). Orographic precipitation is well documented and central to determining the amount of snow water equivalent (SWE) in mountainous regions. The Sierra Nevada, a major barrier to land-falling storms from the Pacific, is ideally oriented to produce orographic precipitation and exerts a strong influence on the upslope amplification of precipitation and the regional water budget (Pandey et al., 1999). Despite this well-developed conceptual understanding, our ability to apply this knowledge at spatial and temporal scales relevant to questions of regional climate and local water-supply forecasting are limited by lack of accurate precipitation

HESSD
11, 5327–5365, 2014

measurements across mountains (Viviroli et al., 2011). Additionally, long narrow land-falling bands of extra-tropical Pacific water vapor, referred to as atmospheric rivers, frequently deposit large fluxes of orographic precipitation as they ascend over the Sierra Nevada (Neiman et al., 2008; Ralph and Dettinger, 2011). Atmospheric rivers deposit approximately 40 % of total winter snowfall in the Sierra Nevada, linking ocean–atmosphere interactions and the terrestrial water balance (Dettinger et al., 2011; Guan et al., 2012, 2013a).

Current mountain-basin operational SWE estimates are made with a limited set of snow-course and continuous in situ point measurements from snow pillows. Measurements at these index sites are used to develop statistically based runoff estimates for the subsequent spring and summer. While this approach has provided operationally robust predictions in years near the long-term normal; snow accumulation both varies from year to year and changes in response to long-term climatic conditions; and has, in recent decades, trended outside the statistical normal (Milly et al., 2008). Hence our current methods are becoming less reliable and accurate predictions require a more-comprehensive approach to understanding the processes affecting precipitation and the probabilities of extremes (Rahmstorf and Coumou, 2011).

Accurate estimates of the amount and spatial distribution of both precipitation and SWE are essential given the shift toward spatially distributed models for forecasts of runoff, moisture stress and other water-cycle components (Rice et al., 2011; Meromy et al., 2012). Current operational measurements for precipitation and SWE are limited by scale and by the heterogeneity of snow-accumulation processes, and do not provide spatially representative values (Viviroli et al., 2011; Bales et al., 2006). Uncertainty in watershed-scale SWE and precipitation estimates result in part from the lack of measurements at both the rain-snow transition and highest elevations, and the lack of representative measurements across different slopes, aspects and canopy conditions (Molotch and Margulis, 2008).

Remotely sensed snow properties from satellites and aircraft are used in research, and on a limited basis in forecasts. In both cases these measurements can be blended

HESSD
11, 5327–5365, 2014

using statistical or spatially explicit models to produce discharge forecasts (Rice et al., 2011; Molotch et al., 2005; Fassnacht et al., 2003; Bales et al., 2008; Kerkez et al., 2012). A recent review highlighted the promise of aircraft LiDAR measurements for snow-depth mapping at high spatial resolution and vertical accuracy, using repeat snow-on and snow-off LiDAR flights (Deems et al., 2013). The emergence of quality research datasets for snow mapping offers opportunities to assess LiDAR accuracy and coverage in complex, forested terrain, and its potential for providing a much-needed spatial "ground truth" for watershed-scale snow depth (Harpold et al., 2014).

Research reported in this paper was aimed at determining the influences of terrain and orographic precipitation on patterns of seasonal snow accumulation along a 1650-m elevation gradient in the southern Sierra Nevada. Three questions posed in this research were: (i) what is the magnitude of the elevation lapse rate for snow accumulation, (ii) what is the variability in snow accumulation along an elevation gradient, and (iii) to what extent do local terrain and wind redistribution influence this pattern. It was also our aim to evaluate consistancy between LiDAR estimated SWE and prior model-based estimates of accumulated SWE and total precipitation.

2 Methods

Our approach involved analysis of: (i) LiDAR-based snow-depth estimates derived from two LiDAR acquisitions, one when the ground was snow free and one near peak snow accumulation, (ii) continuous ground-based measurements of snow depth, SWE, wind speed and air temperature, plus operational bright-band radar observations, and (iii) model estimates of SWE and precipitation. The LiDAR data were used to estimate snow depth across the study area at a 1-m spatial resolution in open areas without canopy cover. The ground measurements were used in interpreting the spatial patterns and in estimating SWE, and the bright-band radar in determining the rain-snow transition elevation for precipitation events, an important metric for interpreting snow-depth and SWE along elevation gradients.

HESSD
11, 5327–5365, 2014

2.1 Location

Our study area is centered at approximately 36.5° N, 118.7° W and includes the 53.1 km^2 area covered by the two LiDAR flights in the southeastern part of the 135 km^2 Marble Fork of the Kaweah River watershed, located in Sequoia National Park in the southern Sierra Nevada, California (Fig. 1). Elevations of the LiDAR aquisition were 1850–3494 m, with aspects predominantly trending northwest, about orthoganal to the regions southwest prevailing storm tracks. The landfeatures include glaciated lake basins, cirques and stepped plateus at the highest elevations. Soils are charecterized by morain deposits and well drained granitic soils, at the lower elevations, and rock outcrops with pockets of course shallow soil at the higher elevations. The vegetation cover below 3000 m is primarily coniferous forests that transition with increasing elevation from a Giant Sequoia grove through mixed-conifer forests, to Red Fir forests. Above 3000 m are increasing areas of bare rock with subalpine forests and alpine meadows in locations with soil (Fig. 2b).

2.2 LiDAR altimetry

Airborne-scanning LiDAR altimetry was collected by the National Center for Airborne Laser Mapping (NCALM) using an Optech Gemini® ALTM 1233 airborne-scanning laser (Zhang and Cui, 2007). The two campaigns were conducted in the 2010 water year: 21–22 March for snow on, and 15 August for snow off (Harpold et al., 2014). The instrument settings used for acquisition generated an average point density greater than 10 m^{-2}, and a fine-scale beam-sampling footprint of approximately 20 cm (Table 1). Ground points were classified by NCALM through iteratively building a triangulated surface model with discrete points classified as ground and non-ground (Shrestha et al., 2007; Slatton et al., 2007). The nominal horizontal and vertical accuracy for a single flight path are 0.11 and 0.75 m, respectively; but higher accuracy was likely achieved where flight paths overlapped.

HESSD
11, 5327–5365, 2014

A digital surface model (DSM) was created by using first-return points and discarding outliers > 100 m (tallest trees are approximately 85 m) and returns below −0.1 m; where values in the range of −0.1 to 0 m were classified as 0. A continuous-coverage bare-earth digital-elevation model (DEM) was created through kriging of ground points using a linear variogram with a nugget of 15 cm, a sill of 10 m, a range of 100 m, and a search radius of 100 m, where the minimum number of points was 5 (Guo et al., 2010). We used a 1-m gridded model for representing our data, as this is the smallest footprint that most closely matches the expected beam sampling footprint and uncertainty in horizontal accuracy. After interpolation, digital models of mean elevation and point-return density grids were georegistered to a common grid for snow-on and snow-off flights. The average point-return densities were 8 m^{-2} for the surface model and 3 m^{-2} for the bare-earth model. Grids with no point returns in either flight, primarily under forest canopy, were not used.

The accuracy of the LiDAR altimetry was evaluated by using 352 georegistered 6.25 m^{-2} grid samples of the point cloud along the paved highway in the western part of the domain, because the highway is plowed regularly surface heights do not change with snow accumulation. These samples had a bias of +0.05 m and a standard deviation of 0.07 m, which is below the estimated combined two-flight instrumental elevation error of 0.11 m (Xiaoye, 2008; Zhang and Cui, 2007). A possible explanation of the 0.05 m bias for the snow-on flight is that some sections of the road had a small amount of snow remaining after plowing.

A 1-m gridded digital surface model of the vegetation canopy, created by subtracting the DSM from the DEM, was used to create a layer of vegetation canopy ≥ 2 m. In order to accurately determine snow depth, values were further classified into two groups, where snow depth was either greater to or less than the coincident vegetation height. This allowed us to consider for further analysis only snow from open slopes or where it had accumulated in the gaps between trees. To reduce the amount of error we eliminated locations with slopes greater than 55°, warranted by the high number of erroneous values and known issues of vertical inaccuracies due to slope angle

HESSD
11, 5327–5365, 2014

(Schaer et al., 2007; Deems et al., 2013). Additionally, we eliminated areas with rapid annual vegetation growth that had negative snow-depth values (e.g. areas within a wet meadow); and lastly we filtered out areas with open water, buildings, and parking lots where returns were not representative of local snow accumulation. Mean snow depth for each 1-m elevation band with $\geq 100\,m^2$ area was computed from the snow-depth grid. Additionally a 5-m elevation model, aggregated from the 1-m bare-earth model, was produced to remove scaling biases in the analysis of slope and aspect (Kienzle, 2004; Erskine et al., 2006).

2.3 Spatial analysis

To analyze possible correlations between terrain steepness and snow distribution we calculated the first derivative of slope and snow depth, over distances of 5–100 m, using the 1-m mean snow depths and the corresponding mean slope for each 1-m elevation band, computing the correlation at 5–100 m using 5-m steps. Using the derivatives identifies transition areas.

For quantifying the combined effect of slope and aspect on snow depth we indexed aspect on a scale of 1 to −1 using methods adapted from Roberts (1986):

$$V_A = \cos(A - AF) \quad (1)$$

where V_A is the aspect value, A is the azimuth variable, and FA the focal aspect, e.g. 45° for northeast. The aspect value was further scaled by the sine of the slope angle, yielding 0 in flat terrain and approaching 1 as the mean slope increases to 90°:

$$I_A = \sin(S) \cdot V_A \quad (2)$$

where I_A is aspect intensity and S the slope angle. The method of scaling the cosine of aspect by sine of slope is referred to as “northness” (Molotch et al., 2004). Here we expand both concepts to include other aspects as well by centering the maximum value of the cosine on the focal aspect.

HESSD
11, 5327–5365, 2014

2.4 Ground measurements

Meteorological data were obtained from six meteorological stations in the flight area for the period from the first significant snowfall on 3 December 2009 to the LiDAR acquisition date, henceforth referred to as the snow-accumulation period. At these stations temperature was measured using Vaisala HMP-35 and Campbell T-108 sensors, with wind speed and direction measured using RM Young 5103 sensors. All meteorological stations measure hourly average wind speed; and two stations, Wolverton and Panther, recorded maximum wind gusts at 10 s scan intervals. The M3, Topaz, and Emerald Lake stations are managed by the University of California Santa Barbara, Giant Forest is operated by the California Air Resources Board (available at: http://mesowest.utah.edu/, 2014) and Case Mountain is managed by the Bureau of Land Management (available at: http://www.raws.dri.edu/, 2014). The Giant Forest station is located on an exposed shrub-covered slope; the Case Mountain, Wolverton and Panther stations are in forest openings; Emerald Lake is an alpine cirque; and Topaz and M3 are in alpine fell fields.

Wind sensors are between 4.2 and 6.5 m above ground level; and we scaled wind speeds to 10 m using a logarithmic profile to estimate saltation thresholds:

$$V_{10} = V_z \left[\frac{\ln \frac{z_x}{k}}{\ln \frac{z_{10}}{k}} \right] \quad (3)$$

where V_{10} is wind velocity at 10 m, V_z is measured velocity, z is instrument height, and k the site specific roughness length.

To identify periods with the greatest potential for wind redistribution of snow we filtered for times when temperature was below 0 °C and wind velocity above the minimum saltation threshold of 6.7 m s^{-1} established by Li and Pomeroy (1997a).

Snow depth was measured continuously by 26 ultrasonic snow-depth sensors (Judd Communications, Salt Lake City, UT) placed on various slopes, aspects and canopy covers within 300 m of the Panther and Wolverton meteorological stations. These

HESSD
11, 5327–5365, 2014

snow-depth sensors have an effective beam width of 22°, and were mounted 4.6 m above ground level on a steel arm extending 0.9 m from a vertical steel pipe anchored to a U-channel post. This arrangement provided up to a 2.3 m^2 snow-depth observation area over flat bare ground, with sampling area decreasing as snow depth increases.

The LiDAR measurements, plus ground-based snow-density measurements, were used to develop estimates of SWE versus elevation. Paired snow-depth and snow-pillow SWE measurements were part of the California Cooperative Snow Survey network and data were acquired from the California Department of Water Resources (available at: http://cdec.water.ca.gov/, 2014) for all 16 operable stations on the western slope of the southern Sierra Nevada within 100 km north and 50 km south of the study area (Fig. 1). One snow pillow (GNF) is located 2.5 km west-southwest of the LiDAR acquisition area. Daily snow densities were estimated by dividing the daily mean SWE from the snow pillows by snow depth from the collocated ultrasonic depth sensors. To minimize the error from intermittent noise associated with snow pillows we used the daily average SWE and did not consider measurements under a 20-cm SWE threshold. This procedure was necessary because complete snow coverage of the snow pillow is unlikely for shallow snow and the combined uncertainties of depth sensors and snow pillows can yield significant error in density measurements (Johnson and Schaefer, 2002). In addition, accumulated precipitation measurements from Alter shielded Belfort gauges at GNF, QUA and CRL and manually measured daily precipitation from Lodgepole ranger station (Ldg) were compared with SWE measurements to estimate total precipitation (available at: http://cdec.water.ca.gov/, 2014). All instrumental data were formatted, calibrated and gap filled by interpolation or correlation with other sensors and aggregated to daily means prior to analysis (Moffat et al., 2007). Under 1 % of the meteorological data required filtering or gap filling, snow-pillow data required slightly more (< 5 %) and snow depth required up to 20 %. Stations with data gaps > 2 days with no nearby station for interpolation were not used in our analysis.

HESSD
11, 5327–5365, 2014

2.5 Bright-band radar

The hourly consensus of bright-band freezing levels over wind profilers represents the transition elevation where hydrometeors turn from frozen to liquid. This elevation was determined from Doppler-radar bright-band snow-level analysis (White, 2003; Lundquist et al., 2008; White et al., 2009; Ryzhkov and Zrnic, 1998). These data resolved hourly freezing levels of precipitation events from operational bright-band radar observations occurring upstream of the LiDAR-acquisition area. We present data compiled from observations collected over the 2010 water year snow-accumulation period from the three nearest upwind locations, including Punta Piedras Blancas, Lost Hills, and Chowchilla, California (available at: http://www.esrl.noaa.gov/psd/data/, 2014) (Fig. 1).

2.6 Model reanalysis

We calculated spatial SWE from LiDAR snow-depth measurements using mean snow-density measurements from the 16 snow-pillow sites. These values were compared with two scales of the widely used PRISM precipitation estimates, plus SWE estimates from two different MODIS-based SWE reconstruction models (Daly et al., 2008, 1994; Rice and Bales, 2011; Rice et al., 2011). Using the available 4-km and 800-m PRISM model output we summed precipitation for the accumulation period at the spatial extent of the LiDAR acquisition. The 4-km data were monthly for the 2010 water year and the 800-m data were 30-year mean climatology. For comparison, we then calculated the total seasonal precipitation for each 1-m elevation band across the elevation gradient of both data sets, and aggregated values to the resolution of the comparative data.

One reconstruction data set gives 2000–2009 accumulation-period means of the entire Kaweah River watershed, calculated at a 500-m resolution, based on 300-m elevation-bin averages of MODSCAG snowcover data, local ground-based meteorological measurements and a temperature-index snowmelt equation that was

HESSD
11, 5327–5365, 2014

calibrated with snow-pillow data (Rice and Bales, 2013). Fractional snowcover was adjusted for canopy using 2 standard deviations of the elevation-band mean.

The second reconstructed SWE data were developed using the algorithm developed by Molotch (2009) and applied to the Sierra Nevada as described in Guan et al. (2013b). Fractional snowcover was adjusted for canopy using vegetation data from the Global Forest Resource Assesment 2000. The Guan values were a subset taken from a Sierra Nevada wide calculation. The primary difference between this method and the one developed by Rice and Bales (2013) is that the Guan et al. (2013b) method includes an explicit treatment of all radiative and turbulent fluxes, whereas the Rice and Bales (2013) method uses a degree-day melt-flux calculation.

3 Results

3.1 LiDAR-measured snow depth

Of the 53.1-km^2 planer footprint of the LiDAR survey, 0.8 km^2 were over water or in areas that exceeded filter thresholds of the digital surface model (DSM). An additional 0.01 km^2 of area with slope > 55°, roads and buildings, and rapidly growing meadow vegetation were also removed from the analysis. The total snow-covered area where both LiDAR and ground returns were available at a density ≥ 1 m^{-2} was 40.2 km^2, and of this area 5.0 km^2 was under canopy and also eliminated from this analysis. This left an area of 35.2 km^2 remaining for analysis, and of this < 0.2 km^2, mostly below 2300 m, was snow free. Mean snow depth, measured by LiDAR, increased with altitude from 1850 to 3300 m elevation, with depths decreasing above 3300 m (Fig. 2a). Up to 3300 m, snow depth shows a strong correlation with elevation (R^2 = 0.974, p < 0.001), increasing at 15 cm per 100 m elevation, with a steep increase in snow depth at 2000–2050 m. Above 3300 m, snow depth sharply decreased at a rate of −48 cm per 100 m (R^2 = 0.830, p < 0.001). The mean "open" snow-covered area in each 1-m elevation band was 1.7 ha, with a range of 0.1–7.3 ha. Overall, 67 % of the study area (excluding

HESSD
11, 5327–5365, 2014

water or developed areas) was free of canopy, including most of the 5.6 km^2 area above 3300 m. The increase in snow depth with elevation up to 3300 m is accompanied by a decrease in canopy cover with elevation. Canopy cover, based on the canopy-height model, is greater than 40 % below 2600 m, and near zero above 3200 m (Fig. 2b).

3.2 Wind and topographic effects

Hourly average wind speed at the 6 meteorological stations showed that the highest potential for redistributing snow was from the westerly directions, with a few periods of strong winds from the northeast at Topaz (Fig. 3). Winds were highest at the 3 stations above 2800 m and, to a lesser extent, at one lower-elevation station, Giant Forest, which is located in an exposed area free of upwind vegetation. Only five instantaneous gusts over 6.7 $m\,s^{-1}$ were recorded at Panther during the snow-accumulation period, and in one instance at Wolverton; and no hourly averages at these sites were over 6.7 $m\,s^{-1}$.

Snow depths were lowest on the southwest and southeast facing slopes, and highest on the northwest- and northeast-facing slopes (Fig. 2c). This pattern was most pronounced at elevations above 2400 m; and depths were low especially in the southeast between 2300 and 2700 m, which is a small fraction of the area at this elevation (Fig. 2c). The aspect with the least overall area is northeast and the greatest areal aspect representation faces northwest.

The changes in mean snow depth and slope (Fig. 2a and d), over 5–100 m averaging lengths, show an (anti) correlation at −0.16 to −0.36, with the most-negative correlation at 35 m (data not shown). The most-rapid changes in slope with elevation show the least increase in snow depth, this is most evident up to 3300 m, above which the terrain becomes flatter (Fig. 2e).

The combined effects of slope and aspect express the "aspect intensity" (I_A), where higher values represent more terrain at that aspect and/or greater slope angles (Fig. 4a). This analysis reveals the slope- and aspect-feature space of the study area,

HESSD
11, 5327–5365, 2014

where the predominant sloped aspects of north, southwest, west and northwest have positive I_A values. Conversely, south, northeast, east and southeast have negative values closer to zero and are therefore less represented in the study area. At elevations < 2000 m, moderate east- and southeast-facing slopes, indicated by the slightly negative I_A values, quickly rise to steeper north, northwest and west slopes, as indicated by the higher and positive I_A values (Fig. 4a). Near 2400 m, southwest aspects become more predominant than north, as indicated by the crossover in I_A values, and at higher elevations aspect becomes equally represented by west, southwest and northwest, with some southerly aspects (negative north I_A values) above 2800 m (Fig. 4a).

To evaluate the terrain effects secondary to elevation we applied a regression to all snow depths as a function of elevation using the slope (0.15) and intercept (−169) from the snow depth measured by LiDAR at 1850–3300 m (Fig. 4b). The residuals from this regression were then correlated with each of the predominant I_A values (Table 2, Fig. 4c and d). I_A snow-depth anomalies for the lowest elevations (1850–2051 m) were negatively correlated with the southeast, at the mid elevations (2051–3301 m) most positively correlated with the northwest, and at the highest elevations (3300–3494 m) most positively correlated with the southwest (Fig. 4c and d).

3.3 Bright-band radar

The radar-sounding data include 8287 hourly observations (353 missing) from the 3 sites. While individual observations of freezing levels ranged from 200 to 2700 m, the 95th percentile values were in the range of 950–2550 m (Fig. 5). The greatest variability and highest mean freezing level occurred at the coastal station of Punta Piedras, with the lowest values at the furthest-inland station of Chowchilla. This decline in mean freezing levels going from the coast, inland, suggests that the snow level drops as the air mass moves inland. The third quartile of the freezing level of the farthest-inland station, Chowchilla, is 2063 m; this closely tracks the break in the coefficient of variation and correlation between snow depth and elevation observed from LiDAR at

HESSD
11, 5327–5365, 2014

2050 m (Fig. 2a), and the steep increase in snow depth from 1950 to 2050 m elevation (Fig. 2d).

3.4 Ground measurements

Accumulated precipitation and SWE track each other closely at the two higher-elevation sites (CRL and QUA) but at the lowest site measured (GNF) SWE was up to 21 cm less than total precipitation, showing some melt prior to the LiDAR acquisition (Fig. 6). The lowest precipitation at the lowest gauges was 75 cm at GNF (2027 m) and was 72 cm at Ldg (2053 m).

The LiDAR flights were 17 days after peak depth and three weeks before peak SWE (Fig. 7a and b). The mean and standard deviation of snow depth during LiDAR acquisition, recorded by the 42 depth sensors, was 210 ± 38 cm. This was 21 % less than the mean peak depth of 266 ± 44 cm recorded on 4 March. However the mean SWE recorded by the 16 snow pillows during LiDAR acquisition was 82 ± 16 cm, 1 % less than the mean peak SWE of 83 ± 20 cm on 14 April. Two snow pillows, the lowest, Giant Forest (GNF) at 2027 m, and the most southerly, Quaking Aspen (QUA) at 2195 m, reached peak SWE one week before acquisition, on 15 March, and had ablated 9 and 7 % SWE, respectively, prior to the time of the LiDAR acquisition (Fig. 7b). All other snow pillows either gained SWE or ablated < 5 % in the period prior to the snow LiDAR acquisition. Snow depths measured at the snow-pillow sites on the days of the LiDAR flights failed to show the elevation patterns apparent in the LiDAR depths (Fig. 8).

Daily density values calculated for the 16 snow pillows for 1 February to 30 April indicate a general trend of increasing density and consistent intra-site patterns of accumulation and densification corresponding with stormy and clear conditions (Fig. 7). Over the 3-month period, density decreased with each accumulation event and increased through densification as the snowpack settled, metamorphosed and integrated free water from melt or rain. At the time of the LiDAR flights the mean density was $384\,\mathrm{kg\,m^{-3}}$, with a range of $\pm 83\,\mathrm{kg\,m^{-3}}$ and standard deviation

HESSD
11, 5327–5365, 2014

of 42 kg m^{-3}, across the 1036-m elevation range represented in these data. The combined measurement error of snow-pillow and depth-sensor instruments used in the density calculation can be greater than the range of variability reported here (Johnson and Schaefer, 2002). We found low spatial variability in density that showed no significant relationship with elevation at our sites. This observation concurs with other studies of mountain snowpacks finding spatial consistency in the density of mountain snowpacks (Jonas et al., 2009; Mizukami and Perica, 2008).

3.5 Model reanalysis

The 4-km resolution PRISIM data were comprised of 7 grid elements in the study domain, whereas the 800-m product had approximately 4225 grid elements. Both PRISM data show a small upward trend in precipitation with elevation up to about 3300 m and a reversal of this trend at the higher elevations. The 4-km and 800-m PRISM data demonstrate similar magnitudes of increase in precipitation with elevation, 2–3 cm 100 m^{-1} respectively. Because of this small precipitation lapse rate, the PRISM estimates diverge from the LiDAR values below about 2800 m. Total precipitation measured at two locations near the lower extent of the LiDAR footprint during the accumulation period was 72 cm at Ldg (2053 m) and 75 cm at GNF (2027 m) (available at: http://cdec.water.ca.gov/, 2014) (Fig. 1). When compared with the LiDAR SWE estimates on Fig. 9 both stations show slightly more precipitation.

Total precipitation was also measured at two additional snow-pillow sensors, CRL (3170 m) and QUA (2195 m) (Fig. 1). From Fig. 6 it is apparent that snow does not account for all of the precipitation at elevations below 2200 m, but does above this elevation where rain had little influence for the accumulation period prior to the LiDAR flight. Thus the LiDAR data should reflect total precipitation above 2200 m.

The LiDAR SWE and the two reconstructed-snowmelt calculations have similar slopes of about 6 cm 100 m^{-1} (Fig. 9). The calculations from Guan et al. (2013b) most closely match the LiDAR estimates up to 3300 m where those from Rice and

HESSD
11, 5327–5365, 2014

Bales (2013) are offset 20–40 cm but show a slight decrease in depth at the highest elevations. In contrast the two PRISM precipitation models deviate from the LiDAR SWE estimates at elevations below 2800 m and have markedly different slopes.

4 Discussion

The overall increase in snow depth with elevation observed with the LiDAR sensor is consistent with the orographic effect of mountains on precipitation (Roe, 2005; Roe and Baker, 2006). At lower elevations, e.g. below 2050 m, a mix of rain and snow precipitation appears to influence the amount of seasonal snow accumulation. Above 3300 m, the reduced lift over flatter terrain and an exhaustion of precipitable water as storms rise less steeply result in declining snow depths at the higher elevations (Houze Jr., 2012). While these patterns may be unique to the 2010 water year, previous works have shown consistency in the interannual spatial patterns of snow accumulation (Sturm and Wagner, 2010; Deems et al., 2008).

4.1 Rain–snow transition

As other researchers have noted, it is difficult to identify the effects of specific storms on snowpack ablation due to the variability of atmospheric conditions close to the earth's surface (Lundquist et al., 2008). Local SWE measurements are only available at one location below 2050 m (GNF); and this station does show a very small loss of SWE in mid-February as a result of a rain-on-snow event (Fig. 6). Nevertheless, given the expected large storm-to-storm variation in freezing level, the relatively sharp transition in slope of LiDAR-measured snow accumulation at about 2050 m does suggest that in the winter 2010, most precipitation above this elevation fell as snow. The aspect and elevation relationships with snow depth point to the potential for considerable mid-winter melt at mid to lower elevations.

HESSD
11, 5327–5365, 2014

Seasonal snow accumulation at the lowest elevations and on south-facing slopes have greater positive net energy exchange (from radiation or condensation), and are most susceptible to melt during the accumulation period. LiDAR snow-depth results reveal these processes, as snow depth typically deviated from the elevational trend with lower depths on south-facing versus greater depths on north-facing slopes (Fig. 2c).

As Fig. 8 shows, snow depths from snow-pillow sites fail to capture the elevation patterns apparent in the LiDAR data. This pattern is also apparent in the SWE values from the same sites (Fig. 7b). While the shallowest depth is registered at the lowest-elevation site (GNF, 2027 m), where a greater percentage of precipitation falls as rain, the other sites do not show a consistent increase in depth with elevation.

In dry intercontinental locations, sublimation rates can be in excess of 50 %, but are much lower in the maritime climate of the Sierra Nevada and lowest during the accumulation period (Ellis et al., 2010; Essery and Pomeroy, 2001). Studies conducted at 2800 and 3100 m in the Emerald Lake basin, located in the center of our measurement domain, found net losses due to evaporation and sublimation of < 10 % for the period between 1 December and 1 April (Marks and Dozier, 1992; Marks et al., 1992). In the 2010 water year we consider cumulative loss due to sublimation and snowmelt to be limited (< 10 %) prior to the LiDAR acquisition at all elevation bands, with more melt occurring at the lowest elevations and on the southeast-facing slopes, as indicated by the loss of SWE measured at the low-elevation snow-pillow sites and reduced snow depths on the southeast mid-elevation slopes (Fig. 2c, 6, and 7).

4.2 Wind redistribution and aspect intensity

The high-spatial-resolution LiDAR snow-depth measurements point to two possible controls of wind redistribution on snow. While wind patterns from a single station may be a poor indicator of the wind fields influencing snow redistribution across the entire domain, we expect snow transport by wind to be coarsely defined by the consensus of the local station's wind direction when temperatures are below zero within 24 h of a snowstorm (Figs. 1 and 3). However, the Topaz Lake station, located in smooth

HESSD
11, 5327–5365, 2014

terrain with limited upwind influence, may best represent the wind patterns of the free atmosphere and predominant southwest storm winds. We attribute the inconsistent wind direction of other stations to the terrain induced turbulence of the free atmosphere upwind of the stations. The M3 and Emerald Lake sites have upwind obstacles, and the Wolverton and Panther stations have low wind speeds, reflecting the muting effect of tall forest cover on wind speed and consequently snow redistribution (Fig. 3).

Consistent with prevailing winds from the southwest, we observed more accumulation on the northeast slopes and less on the southwest; however, in our domain northeast has the least total area of all aspect quadrants and hence these areas may be underrepresented in the analysis (Fig. 2c).

Residuals from a linear trend plotted by I_A suggest that the steeper, northwest-facing slopes at the mid elevations and northerly slopes at the lowest elevations show the greatest snow depths, likely due to the combined effects of wind deposition and lower radiation influx (Fig. 4c and d). Conversely, low- to mid-elevation slopes prone to the combined effects of ablation and wind erosion have the least snow. Elevations over 3300 m showed the greatest negative departure from the overall orographic trend, likely due to the southwest-to-northeast trending terrain flattening out and no longer providing the necessary lift for the same rate of adiabatic cooling (Figs. 2 and 4). Wind-driven sublimation may also play a role at the higher elevations where the highest wind velocities and thus greatest suspension of snow occur (Figs. 3). These findings suggest that departures from the overall orographic trend can be observed in the elevation profile using I_A; but there are limitations to the approach used here.

The variable I_A combines the influences of slope and aspect, and serves as a proxy for several processes affecting snow depth, e.g. radiation, upslope orographic deposition and potentially wind and gravitational redistribution. As a result some local anomalies, such as deep-snow-patch development, are likely masked when considering topography and snow depth as elevation-band means. It is also possible that there is limited utility in extrapolating prevailing winds from meteorological stations to predict localized effects of wind on snow redistribution because of the turbulence

HESSD
11, 5327–5365, 2014

from local terrain. Research into the relationship between slope, aspect and wind has revealed that small-scale slope breaks and surface roughness have the most-significant effects on where snow accumulates locally (Li and Pomeroy, 1997b; Winstral et al., 2002; Fang and Pomeroy, 2009; Pomeroy and Li, 2000). While not part of this analysis, classification of downwind terrain has been effective for identifying snow-patch development and persistence of localized wind deposition, offering a deterministic explanation for the spatial stationarity of snow (Winstral et al., 2002; Schirmer et al., 2011). The I_A variable may also be effective for classifying locations where these processes are likely to occur.

4.3 Model comparisons

Although orographic precipitation is a well-documented first-order process, in the Sierra Nevada it is not well described at the watershed to basin scale owing to the very limited availability of ground-based SWE and precipitation measurements. Each set of comparative measurements used in this study provides a different index of orographic response: (i) LiDAR is a one-time snapshot of snow depth; (ii) point SWE data are small samples from highly variable spatial values, (iii) reconstructed snowmelt, or retrospective gridded SWE, reflects precipitation minus evaporation and sublimation; and (iv) PRISM is a retrospective precipitation estimate, based largely on lower-elevation stations. Nevertheless these complementary data offer spatially relevant indices of seasonally accumulated precipitation. The less-steep increase in precipitation with elevation seen in the two PRISM profiles versus the LiDAR results are thought to be primarily due to the limited number of mountain stations used to calculate the PRISM trends. SWE loss from ablation and rain versus snowfall are important components of the observed LiDAR lapse rates at lower elevations, particularly below 2050 m; these processes should have only a small influence above that elevation. Evidence for this can be seen in three locations of coincident SWE and cumulative precipitation measurements (Fig. 6). The accumulated SWE and total precipitation at the two higher-elevation stations, CRL and QUA, are in close agreement; and the

HESSD
11, 5327–5365, 2014

lowest station, GNF, shows 21 cm more total precipitation and slight loss of SWE on the date of LiDAR acquisition, demonstrating that measurable rain and melt occurred at the site. In addition, a precipitation station in the Kaweah basin near the LiDAR footprint (Ldg, 2053 m) had an accumulation-period total of 72 cm, higher than the LiDAR SWE estimate and lower than both PRISM estimates for the same time period (Fig. 9). The difference in annual precipitation at these sites versus annual SWE accumulation reflects in part the contribution of both rain and snow and mid-winter melt at this elevation. Thus, divergence of the PRISM and reconstructed SWE at elevations below 2200 m is expected. Temperature records in the area suggest only a small amount of winter melt at 2100 m, with very little winter melt and precipitation as rain above 2400 m (Rice and Bales, 2013).

The general pattern of SWE reconstructed from snowmelt by Guan et al. (2013) compares well with the LiDAR data, being somewhat higher at the highest elevations, lower in the mid elevations, and similar at the lower elevations. Even though the reconstruction was based on energy-balance modeling, the good match is somewhat surprising given the coarseness of the reconstruction model relative to the complex topography of the basin.

The Rice and Bales (2013) reconstruction, in which snowmelt was indexed to amounts and rates at the snow-pillow sites, has less SWE, particularly at the mid to lower elevations. This offset may stem in part from the higher 106 % of average 2010 seasonal precipitation versus 90 % of average precipitation in the 2000–2009 snowmelt reconstruction period. Further, the reconstructed SWE estimates by Rice and Bales (2013) are based on a temperature-index calculation, versus a full energy-balance approach by Guan et al. (2013).

Also, some offset in both reconstructed SWE estimates may reflect a bias in snow-covered-area estimates, which have a 500-m spatial resolution and are heavily influenced by canopy. That is, the LiDAR data represent open areas, and the reconstructed SWE values represent the full domain, but are empirically corrected for canopy.

HESSD
11, 5327–5365, 2014

5 Conclusions

The current results show elevation as the primary determinant of snow depth near the time of peak accumulation over 1650 m on the west slope of the southern Sierra Nevada. LiDAR data reveal patterns potentially associated with orographic processes, mean freezing level, slope, terrain orientation and wind redistribution. Snow depth increased approximately 15 cm per 100 m elevation from snow line to about 3300 m and, equivalent to approximately 6 cm SWE per 100 m elevation. This lapse rate is nearly equal to the SWE-reconstruction approach, but higher than the widely used PRISM precipitation data. Localized departures from this trend of +30 to −140 cm from the km-scale pattern of linear increase with elevation are seen in an elevation profile of 1-m elevation bands. Interestingly, snow depth decreased by approximately 48 cm per 100 m elevation from 3300 to 3494 m elevation. Both PRISM and SWE reconstructions show a leveling off or reductions in SWE at higher elevations as well.

The characterization of snow depth and SWE elevation lapse rates is unique given the high accuracy and high spatial resolution of these data. Moreover, the analysis of the residuals from this elevational trend reveals the role of aspect as a controlling factor, highlighting the importance of solar radiation and wind redistribution with regard to snow distribution. While previous works have come to similar conclusions, the use of LiDAR data reveals these signals in a spatially explicit manner. As LiDAR data become more available, the analyses performed here provide a framework for evaluating the sensitivity of snow-distribution patterns to variability in location and climate.

Acknowledgements. Research was supported by the National Science Foundation (NSF), through the Southern Sierra Critical Zone Observatory (EAR-0725097) and NSF grants (EAR 1141764, EAR 1032295, EAR 0922307), a fellowship for the first author from the Southern California Edison Company and a seed grant through Lawrence Livermore National Laboratory (6766). Supplemental support was also provided by T. Painter and NASA project NNX10A0976G. We acknowledge the comments from J. Fernandez Diaz, M. Conklin, M. Goulden, R. Rice, C. Riebe, and T. Harmon and thank J. Sickman and J. Melack for providing meteorological data.

HESSD
11, 5327–5365, 2014

References

Anderson, R. G. and Goulden, M. L.: Relationships between climate, vegetation, and energy exchange across a montane gradient, J. Geophys. Res., 116, G01026, doi:10.1029/2010jg001476, 2011.

Bales, R. C., Molotch, N. P., Painter, T. H., Dettinger, M. D., Rice, R., and Dozier, J.: Mountain hydrology of the western United States, Water Resour. Res., 42, W08432, doi:10.1029/2005WR004387, 2006.

Bales, R. C., Dressler, K. A., Imam, B., Fassnacht, S. R., and Lampkin, D.: Fractional snow cover in the Colorado and Rio Grande basins, 1995–2002, Water Resour. Res., 44, W01425, doi:10.1029/2006wr005377, 2008.

Barnett, T. P., Pierce, D. W., Hidalgo, H. G., Bonfils, C., Santer, B. D., Das, T., Bala, G., Wood, A. W., Nozawa, T., Mirin, A. A., Cayan, D. R., and Dettinger, M. D.: Human-induced changes in the hydrology of the western United States, Science, 319, 1080–1083, doi:10.1126/science.1152538, 2008.

Daly, C., Neilson, R. P., and Phillips, D. L.: A statistical topographic model for mapping climatolological precipitation over mountainous terrain, J. Appl. Meteorol., 33, 140–158, doi:10.1175/1520-0450, 1994.

Daly, C., Halbleib, M., Smith, J. I., Gibson, W. P., Doggett, M. K., Taylor, G. H., Curtis, J., and Pasteris, P. P.: Physiographically sensitive mapping of climatological temperature and precipitation across the conterminous United States, Int. J. Climatol., 28, 2031–2064, doi:10.1002/joc.1688, 2008.

Deems, J. S., Fassnacht, S. R., and Elder, K. J.: Interannual Consistency in Fractal Snow Depth Patterns at Two Colorado Mountain Sites, J. Hydrometeorol., 9, 977–988, doi:10.1175/2008jhm901.1, 2008.

Deems, J. S., Painter, T. H., and Finnegan, D. C.: Lidar measurement of snow depth: a review, J. Glac., 59, 467–479, doi:10.3189/2013JoG12J154, 2013.

Dettinger, M. D., Ralph, F. M., Das, T., Neiman, P. J., and Cayan, D. R.: Atmospheric Rivers, Floods and the Water Resources of California, Water, 3, 445–478, 2011.

Earman, S. and Dettinger, M.: Potential impacts of climate change on groundwater resources – a global review, Journal of Water and Climate Change, 2, 213–229, 2011.

HESSD
11, 5327–5365, 2014

Ellis, C. R., Pomeroy, J. W., Brown, T., and MacDonald, J.: Simulation of snow accumulation and melt in needleleaf forest environments, Hydrol. Earth Syst. Sci., 14, 925–940, doi:10.5194/hess-14-925-2010, 2010.

Erskine, R. H., Green, T. R., Ramirez, J. A., and MacDonald, L. H.: Comparison of grid-based algorithms for computing upslope contributing area, Water Resour. Res., 42, W09416, doi:10.1029/2005wr004648, 2006.

Essery, R. and Pomeroy, J. W.: Sublimation of snow intercepted by coniferous forest canopies in a climate model, in: Proceedings of the Sixth International Association of Hydrologic Sciences Assembly at Maastricht, the Netherlands, Soil-Vegetation-Atmosphere Transfer Schemes and Large-Scale Hydrological Models, IAHS Publication 270, 343–347, 2001.

Fang, X. and Pomeroy, J. W.: Modelling blowing snow redistribution to prairie wetlands, Hydrol. Process., 23, 2557–2569, doi:10.1002/hyp.7348, 2009.

Fassnacht, S. R., Dressler, K. A., and Bales, R. C.: Snow water equivalent interpolation for the Colorado River Basin from snow telemetry (SNOTEL) data, Water Resour. Res., 39, 1208, doi:10.1029/2002WR001512, 2003.

Galewsky, J.: Rain shadow development during the growth of mountain ranges: An atmospheric dynamics perspective, J. Geophys. Res., 114, F01018, doi:10.1029/2008JF001085, 2009.

Guan, B., Waliser, D. E., Molotch, N. P., Fetzer, E. J., and Neiman, P. J.: Does the Madden-Julian Oscillation Influence Wintertime Atmospheric Rivers and Snowpack in the Sierra Nevada?, Mon. Weather Rev., 140, 325–342, 2012.

Guan, B., Molotch, N. P., Waliser, D. E., Fetzer, E. J., and Neiman, P. J.: The 2010/2011 snow season in California's Sierra Nevada: Role of atmospheric rivers and modes of large-scale variability, Water Resour. Res., 49, 6731–6743, doi:10.1002/wrcr.20537, 2013a.

Guan, B., Molotch, N. P., Waliser, D. E., Jepsen, S. M., Painter, T. H., and Dozier, J.: Snow water equivalent in the Sierra Nevada: Blending snow sensor observations with snowmelt model simulations, Water Resour. Res., 49, 5029–5046, doi:10.1002/wrcr.20387, 2013b.

Guo, Q., Li, W., Yu, H., and Alvarez, O.: Effects of Topographic Variability and Lidar Sampling Density on Several DEM Interpolation Methods, Photogramm. Eng. Rem. S., 76, 701–712, 2010.

Harpold, A. A., Guo, Q., Molotch, N., Brooks, P. D., Bales, R., Fernandez-Diaz, J. C., Musselman, K. N., Swetnam, T. L., Kirchner, P., Meadows, M., Flanagan, J., and Lucas, R.: LiDAR-Derived Snowpack Datasets From Mixed Conifer Forests Across the Western U.S., Water Resour. Res., 50, 2749–2755, doi:10.1002/2013WR013935, 2014.

HESSD
11, 5327–5365, 2014

Houze Jr., R. A.: Orographic effects on precipitating clouds, Rev. Geophys., 50, RG1001, doi:10.1029/2011RG000365, 2012.
Johnson, J. B. and Schaefer, G. L.: The influence of thermal, hydrologic, and snow deformation mechanisms on snow water equivalent pressure sensor accuracy, Hydrol. Process., 16, 3529–3542, doi:10.1002/hyp.1236, 2002.
Jonas, T., Marty, C., and Magnusson, J.: Estimating the snow water equivalent from snow depth measurements in the Swiss Alps, J. Hydrol., 378, 161–167, doi:10.1016/j.jhydrol.2009.09.021, 2009.
Kerkez, B., Glaser, S. D., Bales, R. C., and Meadows, M. W.: Design and performance of a wireless sensor network for catchment-scale snow and soil moisture measurements, Water Resour. Res., 48, W09515, doi:10.1029/2011wr011214, 2012.
Kessler, M. A., Anderson, R. S., and Stock, G. M.: Modeling topographic and climatic control of east-west asymmetry in Sierra Nevada glacier length during the Last Glacial Maximum, J. Geophys. Res., 111, F02002, doi:10.1029/2005jf000365, 2006.
Kienzle, S.: The Effect of DEM Raster Resolution on First Order, Second Order and Compound Terrain Derivatives, Transactions in GIS, 8, 83–111, doi:10.1111/j.1467-9671.2004.00169.x, 2004.
Li, L. and Pomeroy, J. W.: Estimates of threshold wind speeds for snow transport using meteorological data, J. Appl. Meteorol., 36, 205–213, doi:10.1175/1520-0450, 1997a.
Li, L. and Pomeroy, J. W.: Probability of occurrence of blowing snow, J. Geophys. Res. Atmos., 102, 21955–21964, doi:10.1029/97jd01522, 1997b.
Lundquist, J. D., Dettinger, M. D., and Cayan, D. R.: Snow-fed streamflow timing at different basin scales: Case study of the Tuolumne River above Hetch Hetchy, Yosemite, California, Water Resour. Res., 41, W07005, doi:10.1029/2004wr003933, 2005.
Lundquist, J. D., Neiman, P. J., Martner, B., White, A. B., Gottas, D. J., and Ralph, F. M.: Rain versus snow in the Sierra Nevada, California: Comparing Doppler profiling radar and surface observations of melting level, J. Hydrometeorol., 9, 194–211, doi:10.1175/2007jhm853.1, 2008.
Marks, D. and Dozier, J.: Climate and Energy Exchange at the Snow Surface in the Alpine Region of the Sierra-Nevada. 2. Snow Cover Energy-Balance, Water Resour. Res., 28, 3043–3054, doi:10.1029/92wr01483, 1992.

HESSD
11, 5327–5365, 2014

Marks, D., Dozier, J., and Davis, R. E.: Climate and Energy Exchange at the Snow Surface in the Alpine Region of the Sierra-Nevada. 1. Metrological Measurements and Monitoring, Water Resour. Res., 28, 3029–3042, doi:10.1029/92wr01482, 1992.
Marks, D., Link, T., Winstral, A., and Garen, D.: Simulating snowmelt processes during rain-on-snow over a semi-arid mountain basin, Ann. Glaciol., 32, 195–202, 2001.
Maxwell, R. M. and Kollet, S. J.: Interdependence of groundwater dynamics and land-energy feedbacks under climate change, Nat. Geosci., 1, 665–669, 2008.
Meromy, L., Molotch, N. P., Link, T. E., Fassnacht, S. R., and Rice, R.: Subgrid variability of snow water equivalent at operational snow stations in the western USA, Hydrol. Process., 27, 2383–2400, 2012.
Milly, P. C. D., Betancourt, J., Falkenmark, M., Hirsch, R. M., Kundzewicz, Z. W., Lettenmaier, D. P., and Stouffer, R. J.: Climate Change: Stationarity Is Dead: Whither Water Management?, Science, 319, 573–574, doi:10.1126/science.1151915, 2008.
Mizukami, N. and Perica, S.: Spatiotemporal Characteristics of Snowpack Density in the Mountainous Regions of the Western United States, J. Hydrometeorol., 9, 1416–1426, doi:10.1175/2008jhm981.1, 2008.
Moffat, A. M., Papale, D., Reichstein, M., Hollinger, D. Y., Richardson, A. D., Barr, A. G., Beckstein, C., Braswell, B. H., Churkina, G., Desai, A. R., Falge, E., Gove, J. H., Heimann, M., Hui, D., Jarvis, A. J., Kattge, J., Noormets, A., and Stauch, V. J.: Comprehensive comparison of gap-filling techniques for eddy covariance net carbon fluxes, Agr. Forest. Meteorol., 147, 209–232, 2007.
Molotch, N. P.: Reconstructing snow water equivalent in the Rio Grande headwaters using remotely sensed snow cover data and a spatially distributed snowmelt model, Hydrol. Process., 23, 1076–1089, doi:10.1002/hyp.7206, 2009.
Molotch, N. P. and Margulis, S. A.: Estimating the distribution of snow water equivalent using remotely sensed snow cover data and a spatially distributed snowmelt model: A multi-resolution, multi-sensor comparison, Adv. Water Resour., 31, 1503–1514, doi:10.1016/j.advwatres.2008.07.017, 2008.
Molotch, N. P., Painter, T. H., Bales, R. C., and Dozier, J.: Incorporating remotely-sensed snow albedo into a spatially-distributed snowmelt model, Geophys. Res. Lett., 31, L03501, doi:10.1029/2003GL019063, 2004
Neiman, P. J., Ralph, F. M., Wick, G. A., Lundquist, J. D., and Dettinger, M. D.: Meteorological characteristics and overland precipitation impacts of atmospheric rivers affecting the

HESSD
11, 5327–5365, 2014

West Coast of North America based on eight years of SSM/I satellite observations, J. Hydrometeorol., 9, 22–47, doi:10.1175/2007jhm855.1, 2008.
Pandey, G. R., Cayan, D. R., and Georgakakos, K. P.: Precipitation structure in the Sierra Nevada of California during winter, J. Geophys. Res., 104, 12019–12030, doi:10.1029/1999JD90010, 1999.
Pedersen, V. K., Egholm, D. L., and Nielsen, S. B.: Alpine glacial topography and the rate of rock column uplift: a global perspective, Geomorphology, 122, 129–139, doi:10.1016/j.geomorph.2010.06.005, 2010.
Peterson, D. H., Smith, R. E., Dettinger, M. D., Cayan, D. R., and Riddle, L.: An organized signal in snowmelt runoff over the western United States, J. Am. Water Resour. As., 36, 421–432, 2000.
Pomeroy, J. W. and Li, L.: Prairie and arctic areal snow cover mass balance using a blowing snow model, J. Geophys. Res., 105, 26619–26634, doi:10.1029/2000jd900149, 2000.
Rahmstorf, S. and Coumou, D.: Increase of extreme events in a warming world, P. Natl. Acad. Sci. USA, 109, 1–5, doi:10.1073/pnas.1101766108, 2011.
Ralph, F. M. and Dettinger, M. D.: Storms, floods, and the science of atmospheric rivers, EOS T. Am. Geophys. Un., 92, 265–266, doi:10.1029/2011EO320001, 2011.
Rice, R. and Bales, R. C.: An Assessment of Snowcover in 6 Major River Basins of Sierra Nevada and Potential Approaches for Long-term Monitoring, in: Fall Meeting of the American Geophysical Union, San Francisco, USA, December 2011.
Rice, R. and Bales, R.: Water Qauntity: rain, snow, and temperature, Natural Resource Report, NPS/SEKI/NRR-2013/665.7a, National Park Service, Fort Collins, Colorado, 2013.
Rice, R., Bales, R. C., Painter, T. H., and Dozier, J.: Snow water equivalent along elevation gradients in the Merced and Tuolumne River basins of the Sierra Nevada, Water Resour. Res., 47, W08515, doi:10.1029/2010wr009278, 2011.
Roberts, D. W.: Ordination on the basis of fuzzy set theory, Vegetatio, 66, 123–131, 1986.
Roe, G. H.: Orographic precipitation, Annu. Rev. Earth Pl. Sc., 33, 645–671, doi:10.1146/annurev.earth.33.092203.122541, 2005.
Roe, G. H. and Baker, M. B.: Microphysical and geometrical controls on the pattern of orographic precipitation, J. Atmos., 63, 861–880, doi:10.1175/jas3619.1, 2006.
Ryzhkov, A. V. and Zrnic, D. S.: Discrimination between rain and snow with a polarimetric radar, J. Appl. Meteorol., 37, 1228–1240, doi:10.1175/1520-0450, 1998.

HESSD
11, 5327–5365, 2014

Schirmer, M., Wirz, V., Clifton, A., and Lehning, M.: Persistence in intra-annual snow depth distribution: 1. Measurements and topographic control, Water Resour. Res., 47, W09516, doi:10.1029/2010WR009426, 2011.

Shrestha, R., Carter, W., Slatton, C., and Dietrich, W.: "Research-Quality" Airborne Laser Swath Mapping: The Defining Factors, The National Center for Airborne Laser Mapping, 25 pp., 2007.

Slatton, K. C., Carter, W. E., Shrestha, R. L., and Dietrich, W.: Airborne Laser Swath Mapping: Achieving the resolution and accuracy required for geosurficial research, Geophys. Res. Lett., 34, L23s10, doi:10.1029/2007gl031939, 2007.

Stolar, D., Roe, G., and Willett, S.: Controls on the patterns of topography and erosion rate in a critical orogen, J. Geophys. Res., 112, F04002, doi:10.1029/2006JF000713, 2007.

Sturm, M. and Wagner, A. M.: Using repeated patterns in snow distribution modeling: An Arctic example, Water Resour. Res., 46, W12549, doi:10.1029/2010wr009434, 2010.

Trujillo, E., Molotch, N. P., Goulden, M. L., Kelly, A. E., and Bales, R. C.: Elevation-dependent influence of snow accumulation on forest greening, Nat. Geosci., 5, 705–709, 2012.

Viviroli, D., Archer, D. R., Buytaert, W., Fowler, H. J., Greenwood, G. B., Hamlet, A. F., Huang, Y., Koboltschnig, G., Litaor, M. I., López-Moreno, J. I., Lorentz, S., Schädler, B., Schreier, H., Schwaiger, K., Vuille, M., and Woods, R.: Climate change and mountain water resources: overview and recommendations for research, management and policy, Hydrol. Earth Syst. Sci., 15, 471–504, doi:10.5194/hess-15-471-2011, 2011.

White, A. B., Gottas, D. J., Henkel, A. F., Neiman, P. J., Ralph, F. M., and Gutman, S. I.: Developing a Performance Measure for Snow-Level Forecasts, J. Hydrometeorol., 11, 739–753, 2009.

Winstral, A., Elder, K., and Davis, R. E.: Spatial snow modeling of wind-redistributed snow using terrain-based parameters, J. Hydrometeorol., 3, 524–538, doi:10.1175/1525-7541, 2002.

Xiaoye, L.: Airborne LiDAR for DEM generation: some critical issues, Prog. Phys. Geog., 32, 31–49, doi:10.1177/0309133308089496, 2008.

Zhang, K. and Cui, Z.: Airborne LiDAR data processing and analysis tools – ALDPAT 1.0., available at: http://lidar.ihrc.fiu.edu/lidartool.html, last access: March 2014, 2007.

HESSD
11, 5327–5365, 2014

Table 1. Target parameters and attributes for LiDAR flights.

Flight parameters		Instrument attributes	
altitude AGL	600 m	wavelength	1064 nm
flight speed	65 m s^{-1}	beam divergence	0.25 mrad
swath width	233.62 m	laser PRF	100 kHz
swath overlap	50 %	scan frequency	55 Hz
point density	10.27 m^2	scan angle	±14°
cross track res.	0.233 m	scan cutoff	3°
down track res.	0.418 m	scan offset	0°

HESSD
11, 5327–5365, 2014

Table 2. Regression of snow-depth residuals with aspect intensity (I_A).

Elevation, m	R^2/intercept/slope*			
	North	Northwest	Southwest	West
1850–2050	0.32/−23/124	0.22/−26.4/74.3	**0.34/2.0/−531.4**	0.14/−28/81
2051–3300	0.22/1/102	**0.42/−10/134**	0.00/3/10	0.37/−15/160
3301–3494	0/−68/−260	0.08/−72/594	**0.32/−105/1625**	0.25/−91/1028

* All $p < 0.001$, with exception of north at 3301–3494 m and southwest at 2051–3300 m. The 3 elevations and aspects with the highest R^2 values are in bold.

HESSD
11, 5327–5365, 2014

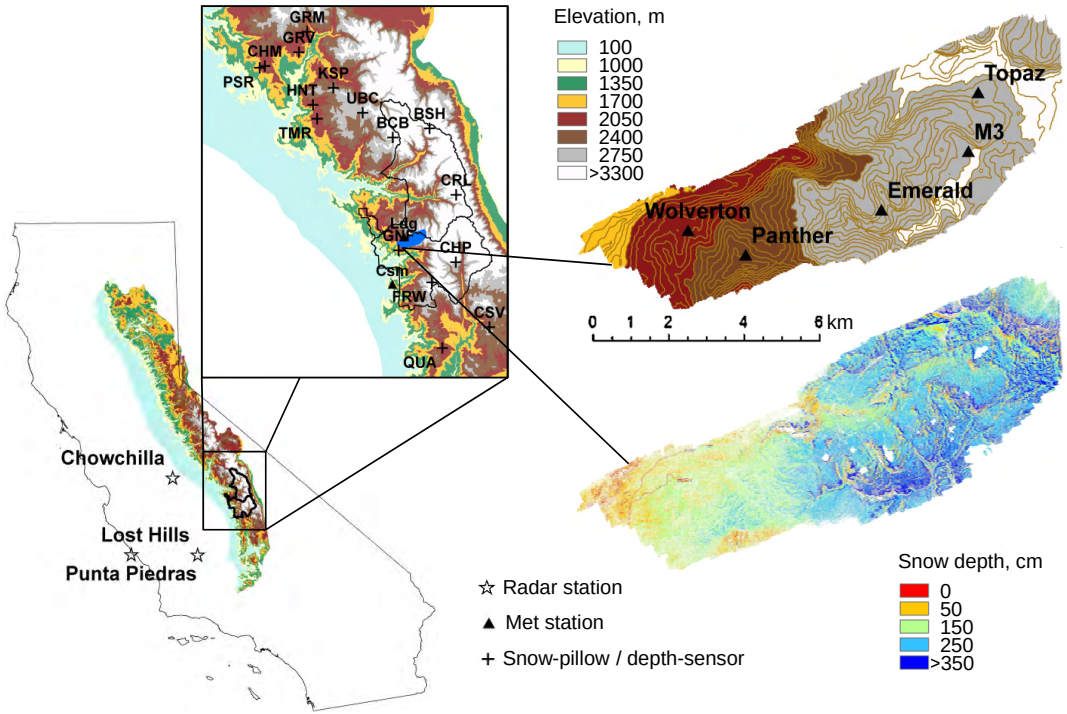

Figure 1. Study area and instrument locations. Left: California with Sierra Nevada, outline of Sequoia and Kings Canyon National Parks and location of radar stations. Center: location of snow sensors, and meteorological stations from north to south: Graveyard Meadow (GRV), Green Mountain (GRM), Chilkoot Meadow (CHM), Poison Ridge (PSR), Kaiser Pass (KSP), Huntington Lake (HNT), Upper Burnt Corral (UBC), Tamarack Summit (TMR), Bishop Pass (BSH), Black Cap Basin (BCB), Charlotte Lake (CRL), Lodgepole met (Ldg), Giant Forest (GNF), Chagoopa Plateau (CHP), Farewell Gap (FRW), Case Mountain met (Csm), Casa Vieja (CSV), and Quaking Aspen (QUA). Upper right: elevation and 50-m contour map with locations of meteorological stations in LiDAR footprint. Bottom right is LiDAR measured 1-m snow depth in areas free of vegetation.

HESSD
11, 5327–5365, 2014

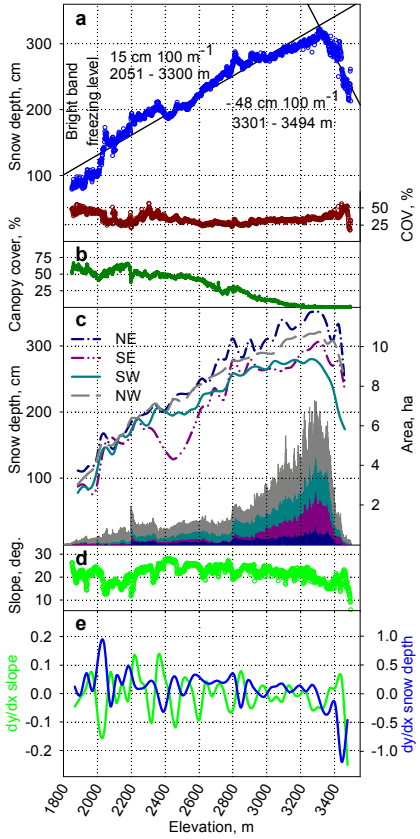

Figure 2. (a) Snow depth (blue) with regression lines and bright-band radar freezing level noted, snow depth percent coefficient of variation (dark red); **(b)** percent canopy cover, **(c)** 35-m running average of mean snow depth and stacked area by elevation for each 90° quadrant of aspect, **(d)** mean slope of 1-m elevation band, and **(e)** first derivative of mean slope (green) and snow depth (blue) over 35-m running average.

HESSD
11, 5327–5365, 2014

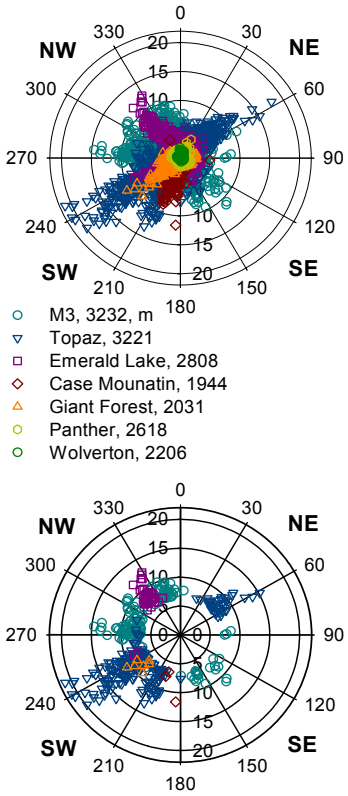

Figure 3. Hourly average wind speed and direction for accumulation period, top; periods with highest probability of snow redistribution bottom, radius scale in m s^{-1}, azimuth in degrees, and north at 0°.

HESSD
11, 5327–5365, 2014

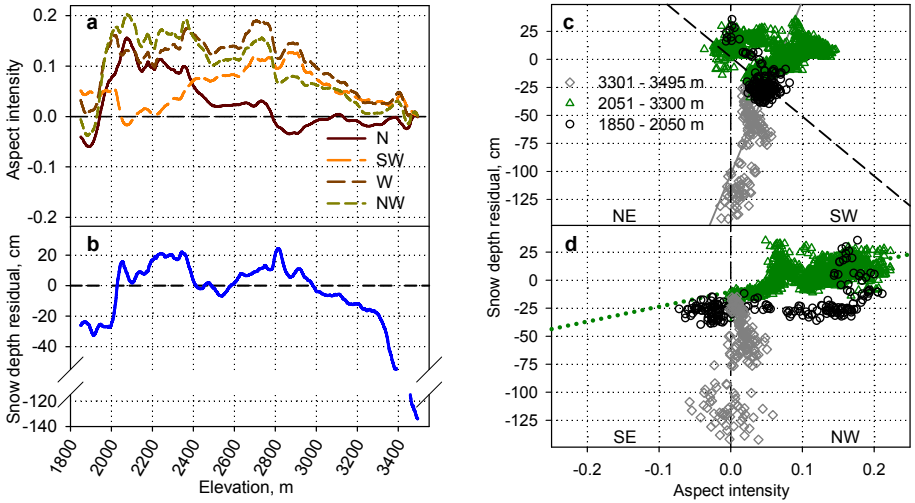

Figure 4. (a) Aspect intensity of LiDAR domain by elevation, **(b)** residuals of mean snow depth using model regression of slope, 1850–3300 m, from Fig. 2a, **(c)** regression of residuals for 1850–2050 m (black, dashed line) and 3301–3494 m (gray, solid line) showing departures from elevation trend for NE and SW aspect intensity, and **(d)** 2051–3300 m (green, dotted line) in SE and NW.

HESSD
11, 5327–5365, 2014

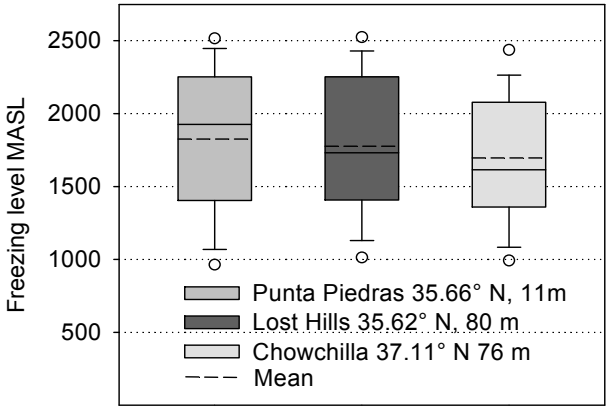

Figure 5. Seasonal-accumulation hourly bright-band freezing level recorded at three wind-profiler stations upwind of the study area; locations shown in Fig. 1. Dots are are 5th and 95th percentile.

HESSD
11, 5327–5365, 2014

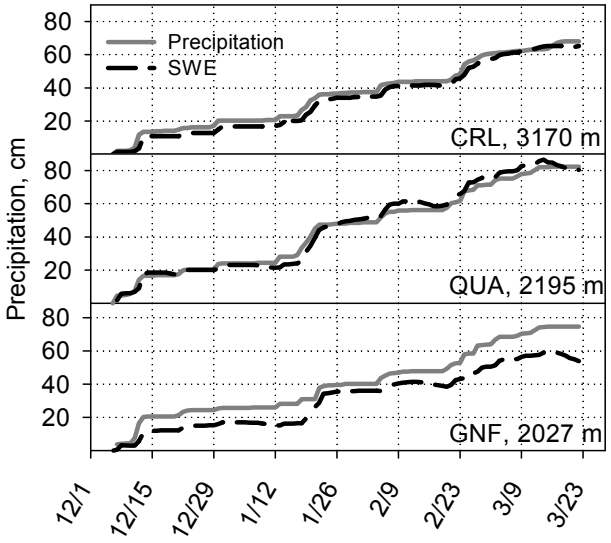

Figure 6. Accumulated gauge precipitation and snow-pillow SWE for the 3 sites with both measurements. Locations are shown in Fig. 1.

HESSD
11, 5327–5365, 2014

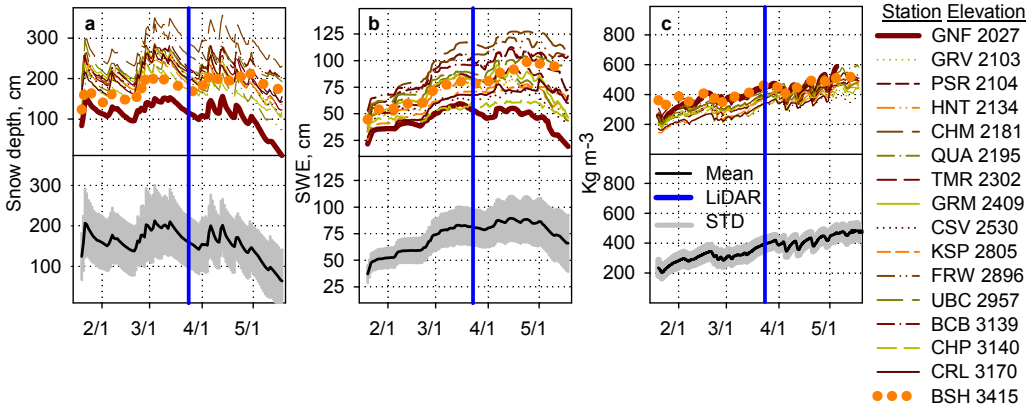

Figure 7. In situ measurements of: **(a)** snow depth, **(b)** SWE, and **(c)** density; for all west-slope snow-pillow and depth sensors in sites located within 1° latitude of study area. Upper panels show data for individual stations, with highest and lowest elevations plotted in bold. Lower panels show mean in black, with ±1 standard deviation shaded in grey; vertical blue line indicates LiDAR acquisition dates. Figure 1 shows station names and locations.

HESSD
11, 5327–5365, 2014

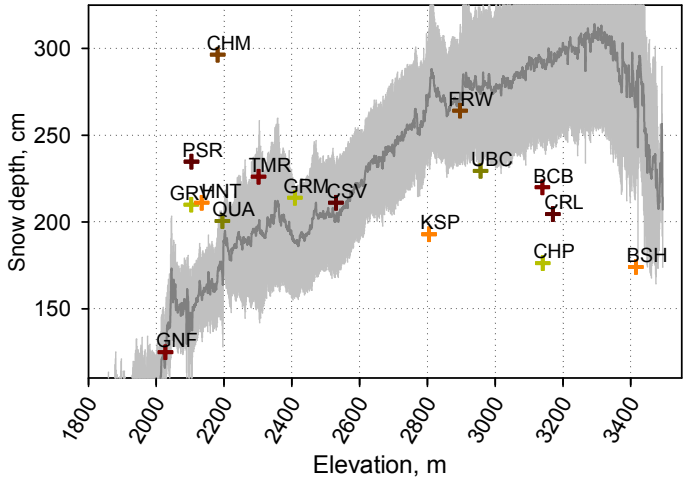

Figure 8. Observed snow depth on the LiDAR acquisition date for all west-slope snow-pillow sites equipped with depth sensors, plotted over mean LiDAR snow depth (dark gray) and 1 standard deviation (light gray). Giant Forest (GNF), Farewell Gap (FRW), and Chagoopa Plateau (CHP) are within 21 km of the measurement domain. Chilkoot Meadow (CHM) and Poison Ridge (PSR) are the sites furthest to the northwest. Locations shown on Fig. 1.

HESSD
11, 5327–5365, 2014

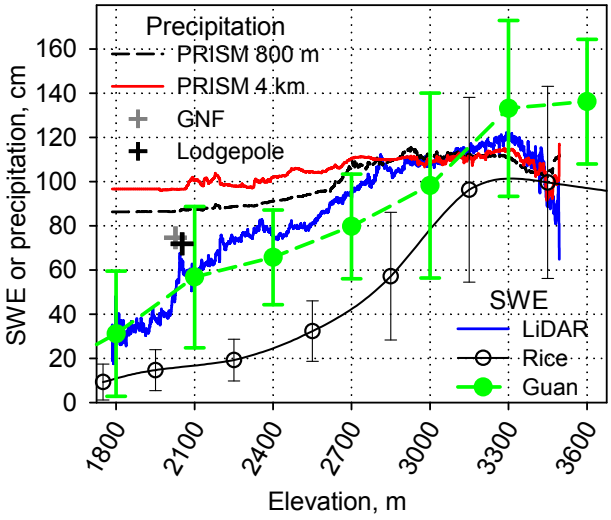

Figure 9. Precipitation and SWE estimates for the Kaweah River watershed, elevation trend for two scales of PRISM total precipitation, LiDAR SWE estimate, and SWE reconstructed from daily snowmelt estimates.

HESSD
11, 5327–5365, 2014